High thermal conductivity and ultrahigh thermal boundary conductance of homoepitaxial AlN thin films EP

View Online   Export Citation   CrossMark

Gustavo Alvarez-Escalante,[1] (ID) Ryan Page,[2] (ID) Renjiu Hu,[1] (ID) Huili Grace Xing,[2,3] (ID) Debdeep Jena,[2,3] (ID) and Zhiting Tian[1,a] (ID)

AFFILIATIONS

[1] Sibley School of Mechanical and Aerospace Engineering, Cornell University, Ithaca, New York 14853, USA
[2] Department of Materials Science and Engineering, Cornell University, Ithaca, New York 14853, USA
[3] School of Electrical and Computer Engineering, Cornell University, Ithaca, New York 14853, USA

[a] Author to whom correspondence should be addressed: zhiting@cornell.edu

ABSTRACT

Wurtzite aluminum nitride (AlN) has attracted increasing attention for high-power and high-temperature operations due to its high piezo-electricity, ultrawide-bandgap, and large thermal conductivity k. The k of epitaxially grown AlN on foreign substrates has been investigated; however, no thermal studies have been conducted on homoepitaxially grown AlN. In this study, the thickness dependent k and thermal boundary conductance G of homoepitaxial AlN thin films were systematically studied using the optical pump–probe method of frequency-domain thermoreflectance. Our results show that k increases with the thickness and k values are among the highest reported for film thicknesses of 200 nm, 500 nm, and 1 μm, with values of 71.95, 152.04, and 195.71 W/(mK), respectively. Our first-principles calculations show good agreement with our measured data. Remarkably, the G between the epilayer and the substrate reported high values of 328, 477, 1180, and 2590 MW/(m^{2}K) for sample thicknesses of 200 nm, 500 nm, 1 μm, and 3 μm, respectively. The high k and ultrahigh G of homoepitaxially grown AlN are very promising for efficient heat dissipation, which helps in device design and has advanced applications in micro-electromechanical systems, ultraviolet photonics, and high-power electronics.

I. INTRODUCTION

Proper control and mitigation of heat is vital for high-power and high-temperature operation.[1] Wide-bandgap (WBG) semiconductors, such as gallium nitride (GaN), and ultrawide-bandgap (UWBG) semiconductors, such as gallium oxide (Ga$_2$O$_3$) and aluminum nitride (AlN), have gained attention due to their potential integration in deep-ultraviolet photonics and in power and radio frequency (RF) electronics.[1] The high-power density sustaining hundreds to thousands of volts causes power devices to exhibit high operating temperatures due to Joule heating, potentially diminishing the device performance and lifetime.[1] Among UWBG semiconductors, the combination of high piezoelectricity, ultrawide bandgap [~6.1 eV, almost as twice as silicon carbide (SiC) and GaN], and one of the largest thermal conductivities k of 340 W/(mK) makes AlN a leading material for advancing

applications in micro-electromechanical systems (MEMS), ultraviolet photonics, and high-power electronics needed to sustain their viability at high temperatures and harsh environments.[2] Furthermore, AlN stands out for its high dielectric strength, ease of deposition and processing (involving low temperatures and nontoxic precursors), and its potential for integration with CMOS devices, MEMS contour mode filters, and film bulk-wave acoustic filters.[3]

Since Slack's pioneering work on k of AlN crystals,[4–6] there has been a follow-up work on k of AlN single crystals[1,7,8] and AlN epilayers on a foreign substrate.[3,4,6,9] However, no thermal studies have been conducted on homoepitaxially grown AlN. Two significant advantages of homoepitaxy are as follows: (1) The G between the epilayer and the substrate is sufficiently high and, in theory, could approach infinity if both the epilayer and the substrate have good quality. (2) The k of the bulk AlN substrate is very high and can efficiently dissipate heat. This paper seeks to elucidate the

thickness dependent cross-plane thermal conductivity k and the thermal conductance G of AlN thin films grown homoepitaxially with the aluminum-assisted surface cleaning method. The optical pump–probe method of frequency-domain thermoreflectance (FDTR) was applied for the measurement, and density functional theory (DFT)-based first-principles calculations were performed for comparison. Good agreement was achieved between experiments and modeling. High k and ultrahigh G values were observed, highlighting the importance of using homoepitaxy for efficient thermal management of AlN-based devices.

II. EXPERIMENTAL SETUP

A. Sample preparation

The AlN films were all grown by molecular beam epitaxy on single crystal (001) oriented AlN substrates while one piece of the AlN substrate served as the reference sample. The AlN bulk substrate underwent *ex situ* solvent cleaning (consisting of 10 min of sonication in acetone and 5 min in 2-propanal).[2,10] The substrates were then cleaned with 1:3 $H_3PO_4 : H_2SO_4$ heated to 70 °C for 5 min, followed by 5-min de-ionized water rinse, finishing with the *ex situ* cleaning.[2,10] They were then transferred into the load-lock chamber of a PA-MBE Veeco GEN10 plasma-MBE system and baked at 200 °C for 8 h.[2,10] *In situ* Al-assisted surface cleaning of the substrates was then performed in the MBE growth chamber at a background pressure of ~10^{-9} Torr without flowing nitrogen gas.[2,10] The substrates were heated up to a thermocouple temperature of 1150 °C and then exposed to an aluminum metal flux of 9.13 nm/min for 30 s.[2,10] The high temperature was held long enough for the deposited Al to desorb; this process of absorption and desorption, which Cho *et al.*[2] invented (i.e. Al-assisted desorption of surface native oxides) and Lee *et al.*[2,10] called Al-polishing, was repeated for several cycles. After these cycles, the surface oxide was completely removed, and after the *ex situ* and *in situ* cleaning, AlN homoepitaxy was performed directly.[2,10] After the first 25 and 50 nm of AlN growth, excess Al was thermally desorbed to make sure that enough Al was present on the surface.[2,10] The remaining AlN layer was then grown with no interruptions, and after the AlN layer was grown, the substrate temperature was increased by ~50 °C to accelerate the desorption of the accumulated excess Al on the surface.[2,10] AFM images reveal a reduction in the root-mean square (rms) surface roughness from 2.1 to 0.5 Å[2,10] with Al-assisted surface cleaning. More importantly, this specific surface preparation technique, invented by Cho *et al.*, leads to no visible growth interface between the bulk AlN substrate and the AlN epitaxial layer as interrogated by transmission electron microscopic studies Ref. 2. Hence, this high-quality nucleation process enables growth of epitaxial AlN films with unprecedented quality. However, the results in this study also suggest there is still room for improvements.

The sample was then coated with a thin film of gold (Au) with a thickness of 80–100 nm. The gold layer was deposited at the Cornell NanoScale Science and Technology Facility (CNF) using the CVC SC4500 Combination Thermal/E-gun Evaporation System with a deposition rate of 1 Å/s. To determine the actual thickness of the deposited Au layer, a P7 Profilometer (stylus-based surface profiler with 0.1 Å vertical resolution) was used at the CNF. A Cascade CPS-06 Four-Point Probe from the Cornell Center for Materials Research (CCMR) was used to determine the electrical conductivity of the Au transducer layer, which was then converted into thermal conductivity with the use of the Wiedemann–Franz law for metals.

B. Frequency domain thermoreflectance (FDTR)

We measured the k and G of thin films using the optical pump–probe method of FDTR. An electro-optic modulator (EOM) induced a sinusoidal intensity modulation on the pump, a 488-nm continuous wave laser (from a signal generated by the lock-in amplifier), creating a periodic heat flux on the sample surface.[11] An unmodulated 532-nm continuous wave probe laser monitored the surface temperature through a change in surface reflectivity, as shown in Fig. 1. We compared the measured phase lag of the balanced probe beam (measured with respect to the reference signal from the lock-in amplifier) and the calculated phase lag of the sample surface temperature, induced by a periodic heat source at the sample surface.[12] The specifications of the experimental setup are provided in the supplementary material.

The samples in this work were modeled as a three-layer system, where each layer includes the volumetric heat capacity c_p, cross-plane thermal conductivity $k_\perp$ and in-plane thermal conductivity $k_\parallel$, layer thickness, and thermal boundary conductances G_1 and G_2, as shown in the inset of Fig. 1. The AlN epitaxial layer thickness ranges from 100 nm to 3 μm for five of our samples, while the sixth sample was used as a reference and does not include the epitaxial layer (i.e., Au deposited on a 574 μm AlN substrate). Au was chosen as a transducer layer to maximize the coefficient of thermoreflectance at the probe wavelength. The measurement of physical properties of individual materials was performed as an inverse problem, minimizing the error between the measured lock-in phase data and the calculated phase through a nonlinear least-squares algorithm.[12]

An example of the phase vs frequency data obtained from FDTR of an average of three runs acquired on one spot location is shown in Fig. S1. The data are in good approximation with the best fit curve obtained from solving the heat diffusion equation. A more comprehensive description of solving this equation is detailed by Schmidt *et al.*[12,13]

C. First-principles calculations

The phonon Boltzmann Transport Equation (BTE) was applied to compute the trend of thickness dependent k of AlN. Note that Xu *et al.*[1] calculated the thickness dependent k of AlN through a simplified BTE method using the Debye approximation for the phonon dispersion of the acoustic modes. In our first-principles calculations, the force constants of AlN are calculated via the Vienna *Ab initio* Simulation Package (VASP)[14] using the projector-augmented-wave method[15] with the generalized gradient approximation proposed by Perdew–Burke–Ernzerhof (PBE)[16] as the exchange–correlation function. First, the AlN wurtzite cell has the optimized lattice parameters a = 3.129 Å and c = 5.018 Å through geometric relaxation, as shown in Fig. S3. The second and third order force constants were then calculated for a 4 × 4 × 4 supercell (256 atoms) of the hexagonal primitive cell. For the BTE calculation, ShengBTE[17] was used to calculate the mode-level phonon group velocity v and phonon–phonon scattering rates τ_{ph} using an iterative scheme with a q-point mesh 32 × 32 × 32, on which the results are fully converged.
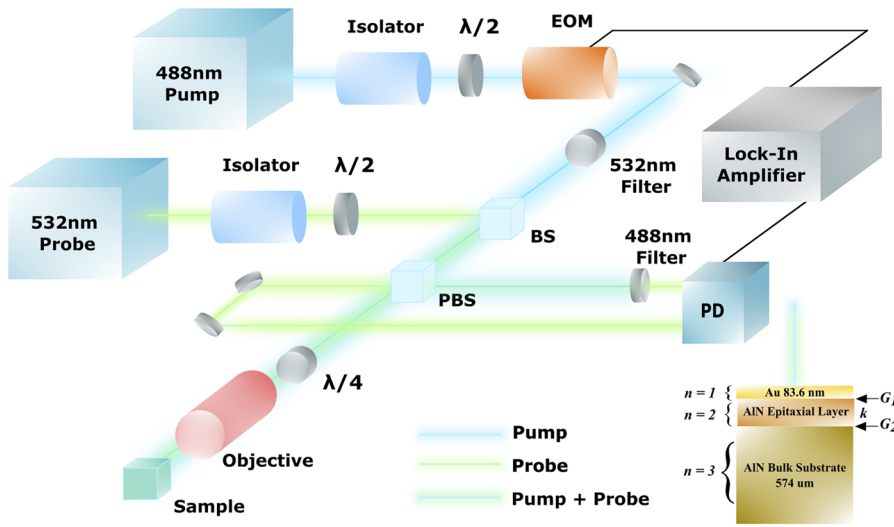
FIG. 1. FDTR setup of a system with two continuous wave lasers where the 488 nm pump laser passed through the electro-optic modulator (EOM), which provided a modulated heat source, while the 532 nm probe laser is aligned coaxially with the BS and focused onto the sample by the objective to monitor the periodic fluctuations in reflectivity at the sample surface. The inset shows the multilayer sample model where each layer includes the volumetric heat capacity c_p, cross-plane $k_\perp$ and in-plane thermal conductivity $k_\parallel$, layer thickness, and thermal boundary conductances G_1 and G_2.

To consider the thermal boundary scattering, we applied the boundary scattering rate to each mode i using the Casimir limit,[18]

$$\frac{1}{\tau_{B,i}} = \frac{d}{v_i}, \qquad (1)$$

where d is the thickness of the AlN epitaxial thin film and v_i is the amplitude of phonon group velocity of mode i. Point defect scattering arises from impurity atoms of carbon (C), silicon (Si), and oxygen (O), and from nitrogen (N) and Al vacancies, with the latter having a more dominant effect in the reduction of k.[1,6] Consequently, we only considered Al vacancy. The point defect scattering rate for each mode i is given by[19]

$$\frac{1}{\tau_{D,i}} = \frac{V}{4\pi v_i^3} \omega_i^4 \sum_j f_j \left(\frac{m - m_j}{m} \right)^2, \qquad (2)$$

where V is the unit cell volume for the wurtzite AlN crystal, ω_i is the angular frequency of mode i, f_j is the fractional concentration of the jth impurity atom, and m and m_j are the masses of the original and jth impurity atoms, respectively. The Al vacancy density is used as a fitting parameter, with values ranging from 2×10^{20} cm^{-3} to no defects.[1] To treat vacancy scattering, the mass was set as six times the mass of the missing atom.[20] Based on Matthiessen's rule, the total scattering rate for each mode satisfies

$$\frac{1}{\tau_i} = \frac{1}{\tau_{ph,i}} + \frac{1}{\tau_{B,i}} + \frac{1}{\tau_{D,i}}. \qquad (3)$$

Ultimately, the thickness dependent k would be the summation of all phonon mode-level contributions,[21]

$$k = \frac{1}{3VN} \sum_i v_i^2 \tau_i \hbar \omega_i \frac{\partial n(\omega_i, T)}{\partial T}, \qquad (4)$$

where N is the total number of q points sampled in the first Brillouin zone, $\hbar$ is the reduced Planck constant, $T = 300$ K, and $n(\omega_i, T)$ is the Bose–Einstein distribution.

III. RESULTS AND DISCUSSION

Table S1 provides a summary of the measured $k_\perp$ and the G_2 of epitaxially grown AlN on bulk AlN of six thin film samples using FDTR. Each entry was the average of three runs on six different spots on the sample (i.e., average of 18 measurements). For the remainder of this paper, $k_\perp$ will be referred to as k. A comparison between the first-principles calculations and the measured thickness dependent k is shown in Fig. 2(a). Both the calculation and the experiment show a clear increasing trend of k with an increasing thickness from 100 nm to 3 μm. The strong size effect indicates that the thickness range is comparable to the phonon mean free path (MFP) of AlN. This is supported by our first-principles calculations that showed a wide range of MFP in AlN from 10 nm to 10 μm [Fig. 2(b)]. For the thickness range we measured, the k has not converged to the bulk value yet.

The commercially purchased bulk AlN sample of 574 μm was used as the substrate for homoepitaxial growth. The measured k of 275.80 W/(mK) agrees with the yellow curve from calculations, indicating a large Al vacancy density ($\sim 2 \times 10^{19}$ cm^{-3}). The agreement of the measured data in the green box and the orange curve in Fig. 2(a) suggests a low Al vacancy density of 4×10^{18} cm^{-3}. One order of magnitude lower than the vacancy level of the substrate iterates the high-quality of the homoepitaxially grown thin films. The 100 and 200 nm samples deviate significantly from the low defect density orange curve to the much higher Al vacancy density purple curves. However, their vacancy levels should not be that high and there must be other scattering mechanisms that were not included in the model.

We noted that a low density of surface pits (i.e., material defects) is inherent to the AlN substrates used in this study, as shown in Fig. S4(a), with an rms = 0.94 nm surface roughness for the 100 nm sample and in Fig. S4(b) for the 200 nm sample. These surface pits, ~ 10 nm in depth, were "healed" over the first ~ 200 nm of AlN MBE growth, as shown in Fig. S4(c), with the reduction in rms = 0.15 nm surface roughness for the 500 nm sample. We consider that these surface pits may cause phonons
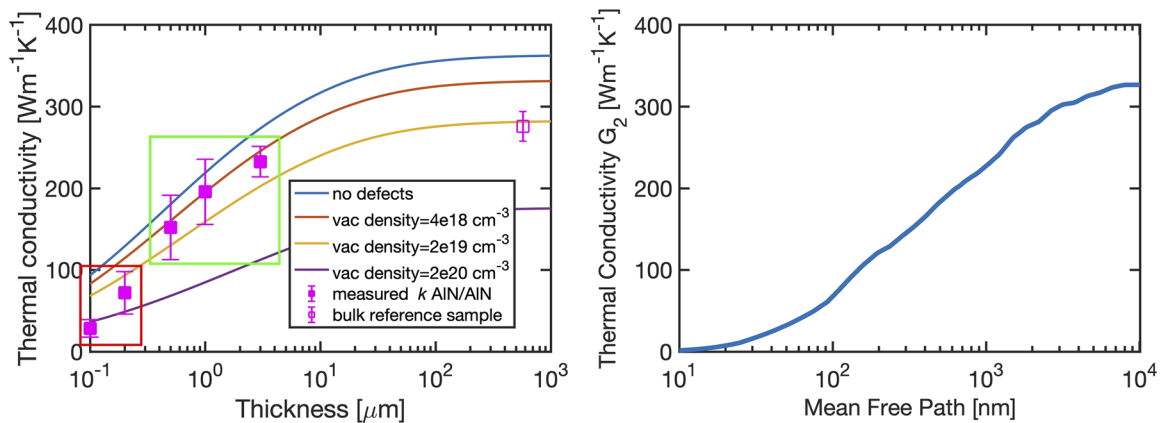
FIG. 2. (a) Comparison between the calculated k based on first-principles calculations and measured k based on FDTR (thickness dependence of AlN). The red square indicates homoepitaxially grown AlN samples impacted by surface pits (i.e., material defects), while the green square indicates homoepitaxially grown AlN samples with a negligible surface pit impact. (b) First-principles calculations of accumulated k vs phonon MFP for pure AlN. The phonon MFP spans a wide range from 10 nm to 10 μm.

to experience more defect scatterings, leading to a shorter effective phonon MFP, thereby a reduction in k. While the point defect (e.g., Al vacancies) is most effective in scattering high-frequency modes, these surface pits might introduce additional scatterings with middle-frequency modes. This is analogous to the strongly suppressed k in rough Si nanowires due to the increased phonon boundary scattering.[22] To rigorously account for the phonon-surface pits scattering would require further investigation with more sophisticated modeling, which is beyond the scope of this work.

A comparison of the measurements from this work and the measurements of the highest room-temperature thermal conductivity of diamond,[23–25] AlN,[9,26–29] and GaN[30,31] thin films is shown in Fig. 3(a). The reported k measurements of this work from 200 nm to 1 μm are among those highest reported for thin films.

A comparison of G_2 measurements from this work and literature values is shown in Fig. 3(b). A G_2 of 230 MW/(m^{2}K) is reported for a GaN film grown on a SiC substrate by radio frequency plasma-assisted MBE.[33] The UWBG β-Ga$_2$O$_3$ grown on diamond with atomic layer deposition at a thickness of 29 nm displays a G_2 of 179 MW/(m^{2}K).[32] For an ideal homoepitaxial growth of AlN, G_2 should theoretically reach infinity based on the diffuse mismatch model. Yet, finite G_2 values indicate the presence of structural or chemical defects at the growth interface and different defect levels between the substrate and the thin films. The relatively lower G_2 of 100 and 200 nm thick films can be attributed to the lower interface quality originating from the surface pits. The ultrahigh thermal conductance G_2 between the homoepitaxial AlN layers and bulk AlN was attained, ranging from 477 MW/(m^{2}K) for the 500 nm sample to 2590 MW/(m^{2}K) for the 3 μm sample. Notably, the G_2 of 1 and
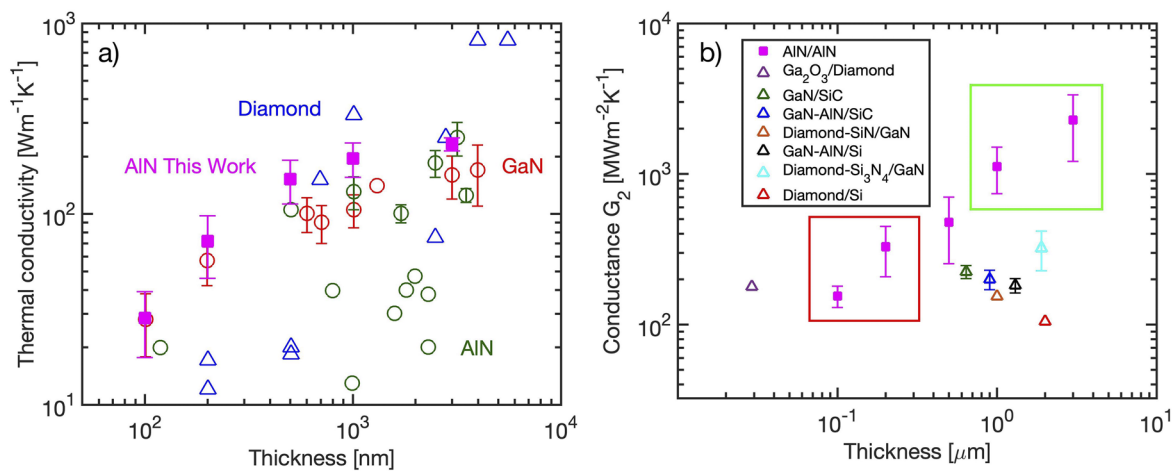

FIG. 3. (a) Comparison of the selected highest room-temperature thermal conductivity of diamond,[9,23–25] AlN,[9,26–29] and GaN[9,30,31] thin films with respect to the thickness. All symbols except the magenta filled squares (which are based on this work) are based on literature values. (b) Comparison of thermal conductance among various WBG and UWBG thin films/substrate reports β-Ga$_2$O$_3$/diamond,[32] GaN/SiC,[33] GaN–AlN/SiC,[34] GaN–AlN/Si,[34] diamond-SiN/GaN,[37] diamond-Si$_3$N$_4$/GaN,[35] diamond/Si,[36] and AlN/AlN (magenta squares, data by FDTR) from this work with respective error bars. The red square indicates homoepitaxially grown AlN samples impacted by surface pits (i.e., material defects). The green square indicates the ultrahigh G_2 of the 1 and 3 μm samples.

3 μm thick epilayers is more than one order of magnitude higher than the state-of-the-art G_2. This ultrahigh G_2 of the thicker epitaxial layers, indicated by the green square in Fig. 3(b), is attributed to (1) homoepitaxial AlN growth and (2) the rms reduction at the epitaxy interface thank to the Al-assisted surface cleaning method, which reduces the interfacial thermal resistance.

IV. CONCLUSIONS

In this work, we investigated the cross-plane thermal conductivity k and thermal boundary conductance G of thin homoepitaxially grown AlN films by implementing the optical pump–probe method of frequency-domain thermoreflectance (FDTR). The samples were prepared with an aluminum-assisted surface cleaning method using molecular beam epitaxy, which results in AlN films with unprecedentedly high crystalline quality. The reported k measurements of this work for 200 nm, 500 nm, and 1 μm are some of the highest reported, with values of 71.95 $\pm$25.90, 152.04 $\pm$39.30, and 195.71 $\pm$39.90 W/(mK), respectively. The phonon Boltzmann transport equation, along with phonon boundary scattering and point defect scattering, was used to calculate the trend of thickness dependent k of AlN, which was in good agreement with our measured data. Moreover, homoepitaxial growth and aluminum-assisted surface cleaning led to some of the highest G reported between the homoepitaxial AlN layers for 200 nm, 500 nm, 1 μm, and 3 μm, with values of 328 $\pm$120, 477 $\pm$223, 1180 $\pm$384, and 2590 $\pm$1070 MW/(m^{2}K), respectively. Our work highlights the great potential of using AlN homoepitaxy for efficient thermal management. The fundamental knowledge developed from this work can be applied to material design and advancing applications in MEMS, ultraviolet photonics, and high-power electronics. It would be compelling to investigate the homoepitaxial k and G thickness and temperature dependence of other UWBG materials.

SUPPLEMENTARY MATERIAL

See the supplementary material for additional details of the FDTR system, sensitivity analysis, sample characterization, limitations of FDTR to measure high thermal conductance, and uncertainty analysis.

AUTHOR DECLARATIONS
Conflict of Interest

The authors declare no conflict of interest.

DATA AVAILABILITY

The data that support the findings of this study are available from the corresponding author upon reasonable request.

REFERENCES

[1] R. L. Xu, M. Muñoz Rojo, S. M. Islam, A. Sood, B. Vareskic, A. Katre, N. Mingo, K. E. Goodson, H. G. Xing, D. Jena, and E. Pop, J. Appl. Phys. **126**, 185105 (2019).

[2] Y. Cho, C. S. Chang, K. Lee, M. Gong, K. Nomoto, M. Toita, L. J. Schowalter, D. A. Muller, D. Jena, and H. G. Xing, Appl. Phys. Lett. **116**, 172106 (2020).

[3] B. E. Belkerk, S. Bensalem, A. Soussou, M. Carette, H. Al Brithen, M. A. Djouadi, and Y. Scudeller, Appl. Phys. Lett. **105**, 221905 (2014).

[4] G. A. Slack and T. F. McNelly, J. Cryst. Growth **42**, 560 (1977).

[5] G. A. Slack, R. A. Tanzilli, R. O. Pohl, and J. W. Vandersande, J. Phys. Chem. Solids **48**, 641 (1987).

[6] G. A. Slack, J. Phys. Chem. Solids **34**, 321 (1973).

[7] A. V. Inyushkin, A. N. Taldenkov, D. A. Chernodubov, E. N. Mokhov, S. S. Nagalyuk, V. G. Ralchenko, and A. A. Khomich, J. Appl. Phys. **127**, 205109 (2020).

[8] Z. Cheng, Y. R. Koh, A. Mamun, J. Shi, T. Bai, K. Huynh, L. Yates, Z. Liu, R. Li, E. Lee, M. E. Liao, Y. Wang, H. M. Yu, M. Kushimoto, T. Luo, M. S. Goorsky, P. E. Hopkins, H. Amano, A. Khan, and S. Graham, Phys. Rev. Mater. **4**, 044602 (2020).

[9] Y. R. Koh, Z. Cheng, A. Mamun, M. S. Bin Hoque, Z. Liu, T. Bai, K. Hussain, M. E. Liao, R. Li, J. T. Gaskins, A. Giri, J. Tomko, J. L. Braun, M. Gaevski, E. Lee, L. Yates, M. S. Goorsky, T. Luo, A. Khan, S. Graham, and P. E. Hopkins, ACS Appl. Mater. Interfaces **12**, 29443 (2020).

[10] K. Lee, Y. Cho, L. J. Schowalter, M. Toita, H. G. Xing, and D. Jena, Appl. Phys. Lett. **116**, 262102 (2020).

[11] K. T. Regner, S. Majumdar, and J. A. Malen, Rev. Sci. Instrum. **84**, 064901 (2013).

[12] A. J. Schmidt, R. Cheaito, and M. Chiesa, Rev. Sci. Instrum. **80**, 094901 (2009).

[13] J. Yang, E. Ziade, and A. J. Schmidt, Rev. Sci. Instrum. **87**, 014901 (2016).

[14] G. Kresse and J. Furthmüller, Comput. Mater. Sci. **6**, 15 (1996).

[15] P. E. Blochl, Phys. Rev. B **50**(24), 17953 (1994).

[16] J. P. Perdew, K. Burke, and M. Ernzerhof, Phys. Rev. Lett. **77**, 3865 (1996).

[17] W. Li, J. Carrete, N. A. Katcho, and N. Mingo, Comput. Phys. Commun. **185**, 1747 (2014).

[18] Z. Tian, K. Esfarjani, J. Shiomi, A. S. Henry, and G. Chen, Appl. Phys. Lett. **99**, 053122 (2011).

[19] A. Sztein, J. Haberstroh, J. E. Bowers, S. P. Denbaars, and S. Nakamura, J. Appl. Phys. **113**, 183707 (2013).

[20] N. A. Katcho, J. Carrete, W. Li, and N. Mingo, Phys. Rev. B **90**, 094117 (2014).

[21] Z. Tian, J. Garg, K. Esfarjani, T. Shiga, J. Shiomi, and G. Chen, Phys. Rev. B **85**, 184303 (2012).

[22] J. Lee, W. Lee, J. Lim, Y. Yu, Q. Kong, J. J. Urban, and P. Yang, Nano Lett. **16**, 4133 (2016).

[23] H. Verhoeven, E. Boettger, A. Flöter, H. Reiß, and R. Zachai, Diamond Relat. Mater. **6**, 298 (1997).

[24] K. E. Goodson, O. W. Käding, M. Rösler, and R. Zachai, J. Appl. Phys. **77**, 1385 (1995).

[25] K. E. Goodson and Y. S. Ju, Annu. Rev. Mater. Sci. **29**, 261 (1999).

[26] K. A. Aissa, N. Semmar, A. Achour, Q. Simon, A. Petit, J. Camus, C. Boulmer-Leborgne, and M. A. Djouadi, J. Phys. D: Appl. Phys. **47**, 355303 (2014).

[27]T. S. Pan, Y. Zhang, J. Huang, B. Zeng, D. H. Hong, S. L. Wang, H. Z. Zeng, M. Gao, W. Huang, and Y. Lin, J. Appl. Phys. **112**, 044905 (2012).

[28]B. E. Belkerk, A. Soussou, M. Carette, M. A. Djouadi, and Y. Scudeller, Appl. Phys. Lett. **101**, 151908 (2012).

[29]C. Duquenne, M. P. Besland, P. Y. Tessier, E. Gautron, Y. Scudeller, and D. Averty, J. Phys. D: Appl. Phys. **45**, 015301 (2012).

[30]T. E. Beechem, A. E. McDonald, E. J. Fuller, A. A. Talin, C. M. Rost, J. P. Maria, J. T. Gaskins, P. E. Hopkins, and A. A. Allerman, J. Appl. Phys. **120**, 095104 (2016).

[31]E. Ziade, J. Yang, G. Brummer, D. Nothern, T. Moustakas, and A. J. Schmidt, Appl. Phys. Lett. **110**, 031903 (2017).

[32]Z. Cheng, V. D. Wheeler, T. Bai, J. Shi, M. J. Tadjer, T. Feygelson, K. D. Hobart, M. S. Goorsky, and S. Graham, Appl. Phys. Lett. **116**, 062105 (2020).

[33]E. Ziade, J. Yang, G. Brummer, D. Nothern, T. Moustakas, and A. J. Schmidt, Appl. Phys. Lett. **107**, 091605 (2015).

[34]J. Cho, Y. Li, D. H. Altman, W. E. Hoke, M. Asheghi, and K. E. Goodson, in Technical Digest IEEE Compound Semiconductor Integrated Circuit Symposium (CSIC), 2012.

[35]Y. Zhou, J. Anaya, J. Pomeroy, H. Sun, X. Gu, A. Xie, E. Beam, M. Becker, T. A. Grotjohn, C. Lee, and M. Kuball, ACS Appl. Mater. Interfaces **9**, 34416 (2017).

[36]Z. Cheng, T. Bai, J. Shi, T. Feng, Y. Wang, M. Mecklenburg, C. Li, K. D. Hobart, T. I. Feygelson, M. J. Tadjer, B. B. Pate, B. M. Foley, L. Yates, S. T. Pantelides, B. A. Cola, M. Goorsky, and S. Graham, ACS Appl. Mater. Interfaces **11**, 18517 (2019).

[37]M. Malakoutian, D. E. Field, N. J. Hines, S. Pasayat, S. Graham, M. Kuball, and S. Chowdhury, ACS Appl. Mater. Interfaces **13**, 60560 (2021).

SUPPLEMENTARY MATERIAL

High Thermal Conductivity and Ultrahigh Thermal Boundary Conductance of Homoepitaxial AlN Thin Films

Gustavo Alvarez-Escalante[1], Ryan Page[2], Renjiu Hu[1], Huili Grace Xing[2,3], Debdeep Jena[2,3], and Zhiting Tian[1] *

1 Sibley School of Mechanical and Aerospace Engineering, Cornell University, Ithaca, NY 14853, USA

2 Department of Materials Science and Engineering, Cornell University, Ithaca, NY 14853, USA

3 School of Electrical and Computer Engineering, Cornell University, Ithaca, NY 14853, USA

* Corresponding author. Email: zhiting@cornell.edu

FDTR Details

An FDTR system is implemented with two continuous-wave lasers: a 488 nm pump and a 532 nm probe, as shown in Fig. 1. The vertically polarized pump beam first travels through an optical isolator. The pump beam is focused into an electro-optic modulator (EOM), and a horizontally polarized beam is transmitted through a beam splitter (BS) and a polarizing beam splitter (PBS). A microscope objective then focuses the beam onto the sample. The lock-in amplifier transmits a periodic signal to the EOM. The EOM then creates a periodic heat flux with a Gaussian spatial distribution on the sample surface. The probe beam first travels through an optical isolator and then through the BS, which coaxially aligns the probe beam with the pump beam. To improve the signal-to-noise ratio at low frequencies, a balanced photodetector (PD) is implemented, composed of two well-matched photodiodes PD1 and PD2. The probe beam is split with a PBS, where one beam (post-sample), which is horizontally polarized, passes through quarter wave-plate and circularly polarized light is focused by a microscope objective onto the sample (on the pump spot) to monitor the periodic fluctuations in reflectivity at the sample surface caused by the oscillating sample temperature. The post-sample is then reflected through the quarter-wave plate and reflected by the PBS to PD1. The other beam (pre-sample) is sent along a matched optical path to PD2. The output currents of PD1 and PD2 are subtracted in the detector and sent through a low noise transimpedance amplifier, removing common mode noise in the probe beam.

The detailed derivation of the mathematical model can be found elsewhere.[1,2] The phase lag of the balanced probe beam, measured with respect to the reference signal from the lock-in amplifier, is compared against the calculated phase lag of the sample surface temperature to a periodic Gaussian heat source at the sample surface.[2] Mathematically, the solution to the calculated phase lag (based on individual materials physical properties of interest, in our case k and G_2) can be expressed as a complex number $Z(\omega_o)$, such that the output of the lock-in amplifier for a reference wave $e^{i\omega_o t}$ is given by

$$Ae^{i(\omega_o t+\phi)} = Z(\omega_o)e^{i\omega_o t} \tag{S1}$$

where ω_o is the modulation frequency, A is the amplitude, and ϕ the phase of the fundamental component of the probe signal with respect to the reference wave.[2]

In the case of continuous-wave pump and probe beams

$$Z(\omega_o) = \beta H(\omega_o) \tag{S2}$$

where β is a factor including the thermoreflectance coefficient of the sample and the power of the pump and probe beams.[2] $H(\omega_o)$ is the thermal frequency response of the sample weighted by the intensity of the probe beam.[2] The weighted sample frequency response, $H(\omega_0)$, is obtained by solving the heat diffusion equation for a Gaussian heat source (the pump beam) impinging on a multilayer stack of materials and weighting the resulting temperature distribution at the top surface by the Gaussian intensity distribution of the probe beam.[2]

As an example, for a single slab of material in the frequency domain, the temperature θ_t and the heat flux f_t on the top side of the slab are related to the temperature θ_b and the heat flux f_b on the bottom side through

$$\begin{bmatrix} \theta_b \\ f_b \end{bmatrix} = \begin{bmatrix} \cosh(qd) & \dfrac{-1}{k_\perp q}\sinh(qd) \\ -k_\perp q\sinh(qd) & \cosh(qd) \end{bmatrix}\begin{bmatrix} \theta_t \\ f_t \end{bmatrix} \tag{S3}$$

where d is the layer thickness, $k_\perp$ the cross-plane thermal conductivity and

$$q^2 = \frac{k_\parallel \mathcal{H}^2 + \rho c i \omega}{k_\perp} \tag{S4}$$

where $\mathcal{H}$ is the Hankel transfer variable, ρ is the density, c is the specific heat capacity, and $k_\parallel$ is the radial thermal conductivity.[2] The heat flux boundary condition at the top layer f_t is given by the Hankel transform of a Gaussian spot with power A_o and $1/e^2$ radius of the pump beam on the surface w_0

$$f_t = \frac{A_0}{2\pi}exp\left(\frac{-\mathcal{H}^2 w_0^2}{8}\right) \tag{S5}$$

Multiple layers are handled by multiplying the matrices for individual layers together

$$\begin{bmatrix} \theta_b \\ f_b \end{bmatrix} = \boldsymbol{M}_n \boldsymbol{M}_{n-1} \dots \boldsymbol{M}_1 = \begin{bmatrix} A & B \\ C & D \end{bmatrix} \begin{bmatrix} \theta_t \\ f_t \end{bmatrix} \tag{S6}$$

where $\boldsymbol{M}_n$ is the matrix for the bottom layer.[2] An interface conductance G is treated by taking the limit as the heat capacity of a layer approaches zero and choosing $k_\perp$ and d such that $G = k_\perp/d$. Since we treat the nth layer as semi-infinite, Eq. (S5) reduces to

$$\theta_t = \frac{-D}{C} f_t \tag{S7}$$

The final frequency $H(\omega)$ in real space is found by taking the inverse Hankel of Eq. (S6) and weighting the results by the probe intensity distribution, which is taken as a Gaussian spot with $1/e^2$ radius of the probe beam on the surface w_1

$$H(\omega_0) = \frac{A_0}{2\pi} \int_0^\infty \mathcal{H}\left(\frac{-D}{C}\right) \exp\left[\frac{-\mathcal{H}^2(w_0^2 + w_1^2)}{8}\right] d\mathcal{H} \tag{S8}$$

This result is inserted into Eq. (S2), where the measurement of individual materials physical properties is performed as an inverse problem, minimizing the error between the lock-in phase data and the phase of Eq. (S2) via a non-linear least-squares algorithm.[2] An example of the phase vs. frequency data obtained from FDTR of an average of three runs acquired on one spot location is shown in Fig. S1.
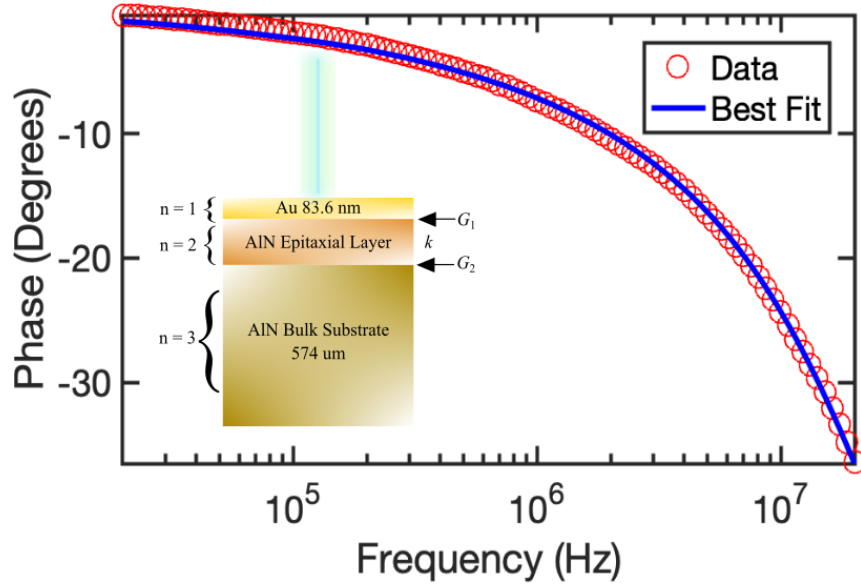
FIG. S1. Phase vs frequency data obtained from FDTR measurements for the 100 nm epitaxial AlN layer on bulk AlN substrate. Measured data shown as red circles are in good approximation to the calculated best fit curve. Inset shows the multilayer sample model where each layer includes the volumetric heat capacity c_p, cross-plane $k_\perp$ and in-plane thermal conductivity $k_\parallel$, layer thickness, and the thermal boundary conductance G_1 and G_2. The best fit is obtained by fitting both $k_\perp$ and G_2.

Sensitivity analysis is used to help us determine which parameters can be fit together. If the sensitivities vary differently over most of the frequency range, then it is possible to extract the parameters from the data set. In the case of AlN, the parameters of interest k and G_2, vary throughout the frequency range 20 kHz-20 MHz and it is possible to extract both parameters simultaneously from one measurement. The sensitivity of the metal-substrate thermal boundary conductance G_1 (i.e., the interface conductance of the Au transducer layer and the AlN epitaxial layer) does not vary greatly with the thickness of the epitaxial AlN layer and is most sensitive at higher frequencies, as shown in Fig. S2(a). The thermal boundary conductance G_2 of the epitaxial AlN and bulk AlN substrate is most sensitive to epitaxial layer thicknesses ranging from 100 nm-500nm, while throughout all our samples, G_2 is most sensitive at higher frequencies, as shown in Fig S2(b). The sensitivity of the epitaxial AlN layer k is most sensitive for samples above 1 μm throughout the frequency range 20 k Hz-20 MHz. For epitaxial layer thickness ranging from 100 nm-500 nm, sensitivity becomes larger after ~1 MHz, as shown in Fig. S2(c).
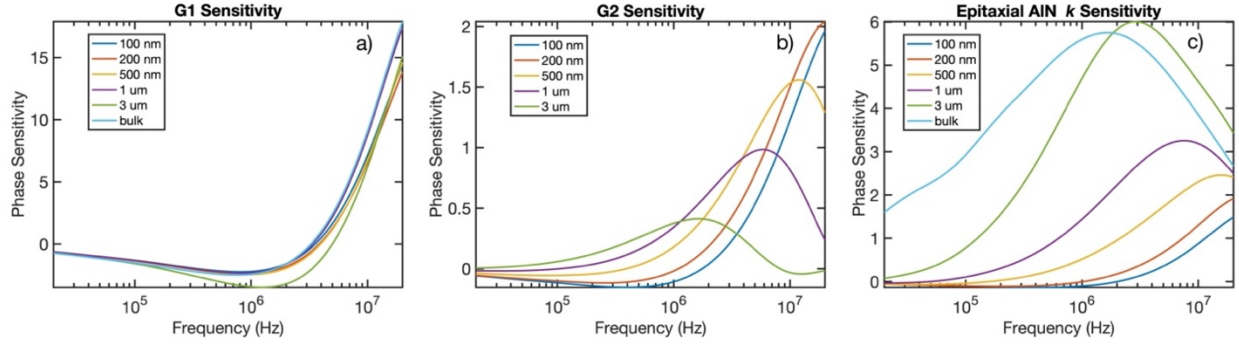
FIG. S2. (a) Sensitivity analysis of the thermal boundary conductance G_1 between the Au transducer layer and the epitaxially grown AlN layer for various thicknesses of the AlN epitaxial layer. (b) Sensitivity analysis of the thermal boundary conductance G_2 between the epitaxially grown AlN layer and the AlN substrate for various thicknesses of the AlN epitaxial layer. (c) Sensitivity analysis of the thermal conductivity k of the AlN epitaxial layer of various thicknesses.

A summary of the thickness-dependent cross-plane thermal conductivity $k_\perp$, which we refer to as k, of epitaxially grown AlN and thermal conductance G_2, between the epitaxially grown AlN and bulk AlN interface, is shown in Table S1.

TABLE S1. Summary of thickness-dependent cross-plane thermal conductivity $k_\perp$ of epitaxially grown AlN and thermal conductance G_2 between the epitaxially grown AlN and bulk AlN interface. Thermal conductivity increases as the thickness increases.

AlN Thickness [μm]	$k_\perp$ [Wm^{-1} K^{-1}]	G_2 [MWm^{-2}K^{-1}]
0.1	28.48	155
0.2	71.95	328
0.5	152.04	477
1	195.71	1180
3	232.59	2590
574	275.80	N/A

AlN structure for DFT calculations

For the first-principles calculations, we used the AlN wurtzite cell with optimized lattice parameters a = 3.129 Å and c = 5.018 Å through geometric relaxation, as shown in Fig S3.

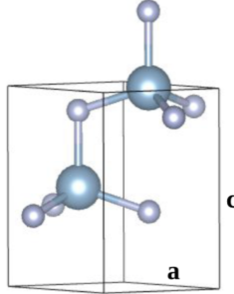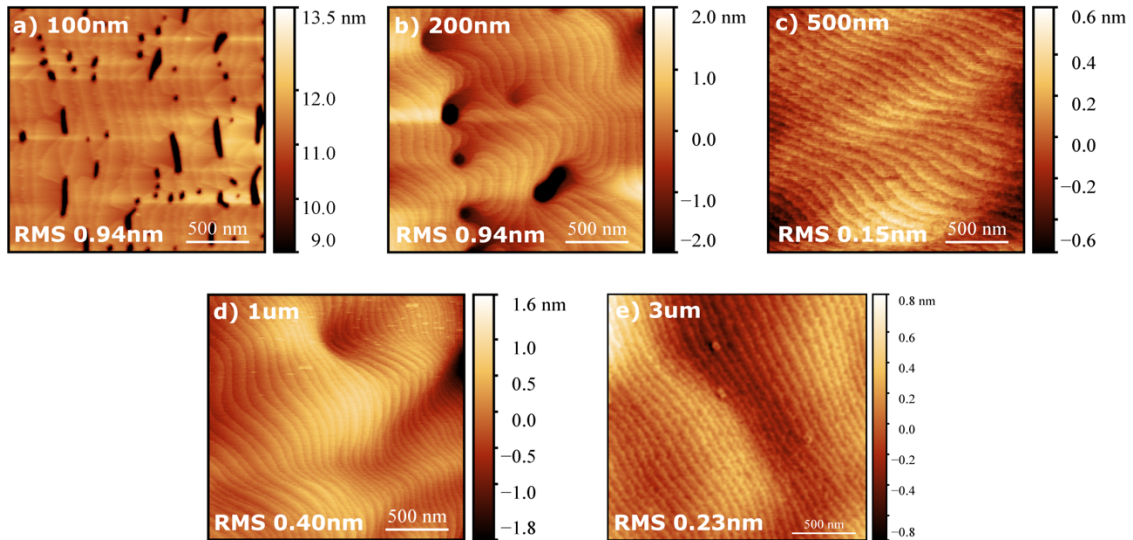FIG. S3. (a) Schematic of AlN wurtzite cell with the optimized lattice parameters a = 3.129 Å and c = 5.018 Å.

FIG. S4. AFM images of epitaxial AlN surface after Al-assisted surface cleaning for samples a) 100 nm, b) 200 nm, c) 500 nm, d) 1 μm, and e) 3 μm with respective root-mean square (RMS) roughness. Surface pits are clear in the 100 nm and 200 nm samples with a large RMS, and are "healed" after sample thicknesses greater than 200 nm showing a lower RMS. These pit features were found to originate from pits already present on the AlN bulk substrates, which can be reduced with improved substrates.

Surface pits are visible in AFM images of the epitaxial AlN surface with a large RMS roughness of 0.94nm for smaller thickness samples, while after 200 nm thickness of the epitaxial AlN the RMS is reduced since the surface pits become "healed", as show in Fig. S4(c). To quantitatively prove the difference between the bulk substrates and the epitaxial layer thin films, we point the reader to two references where secondary-ion mass spectrometry (SIMS) analysis was conducted. The SIMS analyses on the homoepitaxial thin films from the same growth procedure showed that there are differences in impurity levels between the bulk substrates and the high-quality thin films. The detailed analyses can be found elsewhere.[3,4] In summary, SIMS shows a significant reduction of Si and O contamination on the AlN surface by the Al-assisted surface cleaning, enabling greatly improved AlN homoepitaxy.[3,4]

To investigate the limitations of FDTR to measure large G_2, we approached our analysis in two ways; we maintained all parameters as known and only changed G_2 to 1) determine how the calculated phase vs. frequency data changed, and 2) inspect when the residue converged. For our first approach, we selected an expansive range of G_2 from 0-20,000 $MW/(m^2K)$ to verify sites of convergence. From Fig. S5. at low frequencies there is little difference from calculated phase lag and G_2. However, at larger frequencies (specifically, $> 1e6\ Hz$) where the sensitivity to G_2 is high for 1 μm sample, there is a noticeable difference. A zoom-in of this analysis is shown in Fig. S6. where our initial value of 500 $MW/(m^2K)$ and the fitted value of $1180 \pm 384\ MW/(m^2K)$ is highlighted.
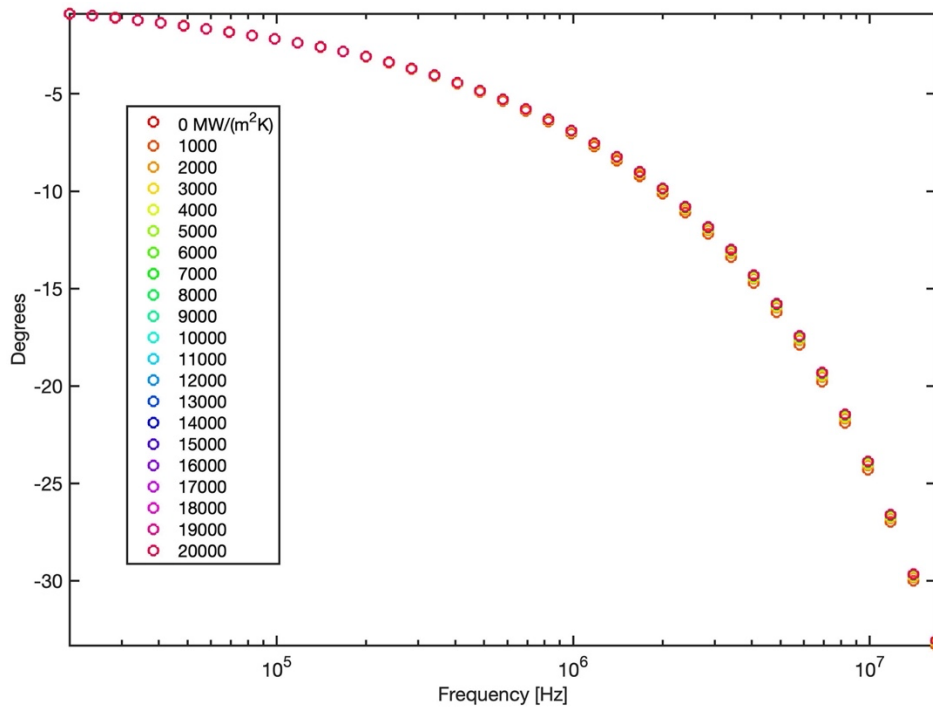

FIG. S5. Calculated phase lag of a non-linear least-squares algorithm based on different G_2 values for the 1 μm sample. Notice at lower frequencies there is almost no distinction of phase dependence on G_2. However, above 1e6 Hz, where the sensitivity to G_2 is high for 1 μm, there is a noticeable difference of phase lag for each G_2.
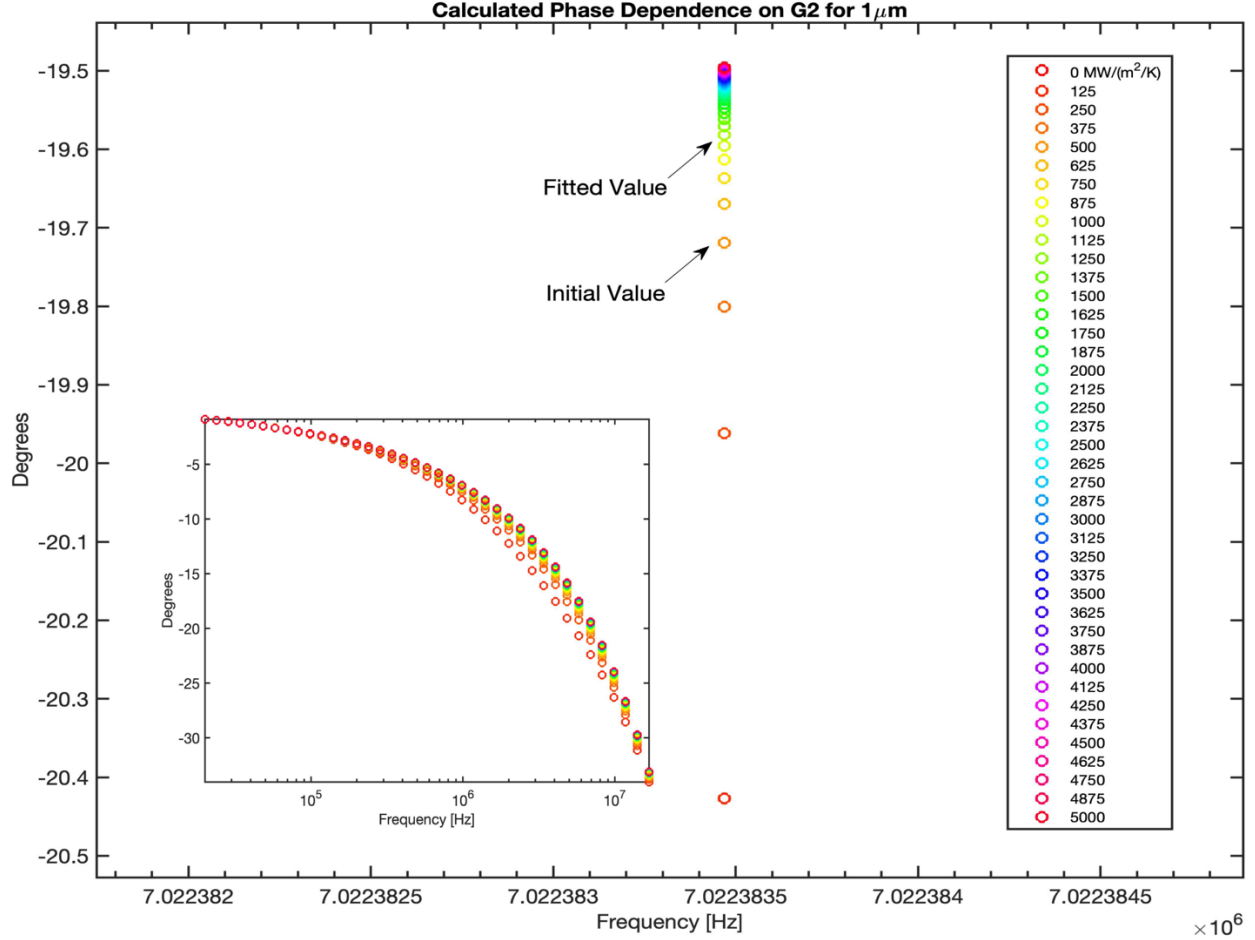
FIG. S6. Calculated phase lag of a non-linear least-squares algorithm based on different G_2 values for the 1 μm sample. Zoom-in near 7e6 Hz where the sensitivity to G_2 is near the max for 1 μm. Notice the initial value G_2 of 500 $MW/(m^2 K)$ and the fitted value of ~1180 $MW/(m^2 K)$, after which the phase lag seems to converge. Inset shows the original plot from which the zoom-in was taken, with G_2 from 0-5000 $MW/(m^2 K)$.

For the second approach, we inspected when the fitting residue converged with respect to G_2. For the 1 μm sample, we determined the summed residue of the calculated vs measured phase lag, plotted against various G_2, as shown in Fig. S7(a). The analysis was performed on six different spot locations on the sample, and each spot consists of the average of three measurements. We determined the difference in residue [Fig. S7(b)], repeated this same procedure for other samples [Fig. S7(c)], and found that approximately after ~5,000 $MW/(m^2 K)$ the difference in residue converges. We believe this indicates the limitations of the FDTR system from accurately determining G_2. Because our fitted values are below the FDTR limit, we think we can still confidently report the actual value.
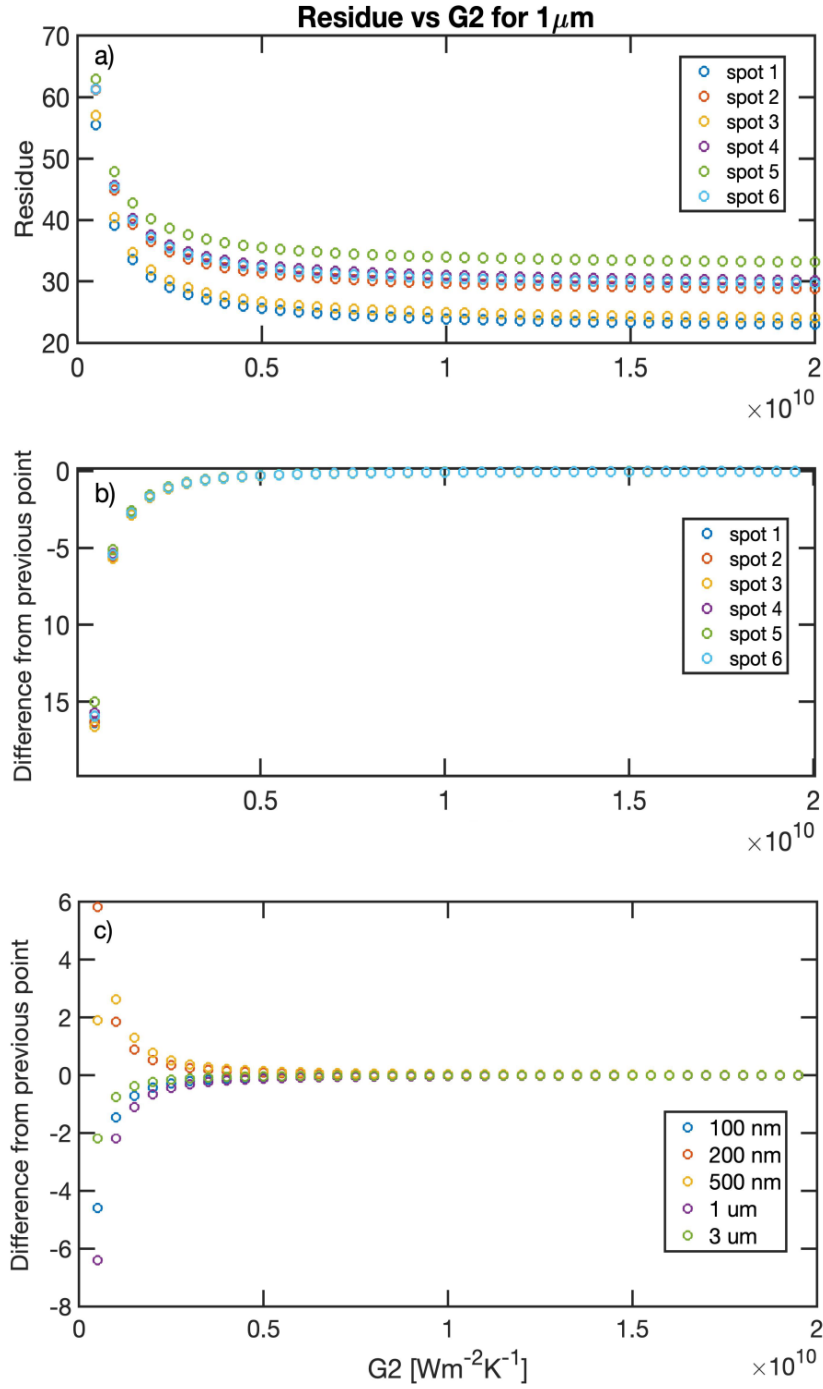
FIG. S7. (a) Summed residue of a non-linear least-squares algorithm based on different G_2 values for the 1 μm sample of data from six different spot locations, and each spot is an average of three measurements. (b) Difference of the next point to the previous point of data from part (a). High differences at lower G_2 due to an inaccurate, unconverged G_2. (c) Difference in residue for various samples. Notice after ~5000 $MW/(m^2K)$ the difference converges.

11

Uncertainty Analysis

We used the analytical method[5] to estimate the uncertainty of our fitted data based on the parameters and measurement. We assumed uncertainty of 3% for the volumetric heat capacity,[5] and 4% for the thicknesses of the Au transducer layer and AlN epilayer. For the thermal conductivity of bulk AlN, we obtained it from the bulk reference AlN substrate (without an epilayer) and determined the thermal conductivity uncertainty of 6.6% using the method below. To explore uncertainties of multiple unknown parameters, Jacobian matrices were used in the calculation. We selected the analytical method because it accumulates uncertainties from the parameters and measurements in the Jacobian matrices. The consideration of correlation would not overestimate the uncertainty.[6] Given the measured signal Φ and known parameter matrix X_C, the variance-covariance matrix of unknown matrix X_U is:

$$var(X_U) = (J_U'J_U)^{-1}J_U'(var(\Phi) + J_C var(X_C)J_C^{-1})J_U(J_U'J_U)^{-1} \tag{S9}$$

Here, $var(\Phi)$ and $var(X_C)$ are the diagonal matrices whose elements are variances of measured signal and known parameters, respectively.[5] J_C and J_U are the Jacobian matrices of known and unknown parameters accordingly with the form:

$$J = \begin{pmatrix} \frac{\partial f(\omega_1, X)}{\partial x_1}|X^* & \cdots & \frac{\partial f(\omega_1, X)}{\partial x_N}|X^* \\ \vdots & \ddots & \vdots \\ \frac{\partial f(\omega_M, X)}{\partial x_1}|X^* & \cdots & \frac{\partial f(\omega_M, X)}{\partial x_N}|X^* \end{pmatrix} \tag{S10}$$

where $f(\omega_M, X)$ is the function to calculate the phase lag between pump and probe signals, ω_i, $i = 1, \cdots, M$ are the frequency that takes the measurement, $x_j, j = 1, \cdots, N$ are the parameters and X^* is the matrix of the fitted data.[5] The diagonal elements of $var(X_U)$ are the variances of the unknown parameters. Thus, this analysis consists of the propagation of errors and the variance among different measurement spots (i.e., the standard error of the six different spot locations, which is incorporated in $var(\Phi)$).

REFERENCES

[1] A.J. Schmidt, X. Chen, and G. Chen, Rev. Sci. Instrum. **79**, 114902 (2008).

[2] A.J. Schmidt, R. Cheaito, and M. Chiesa, Rev. Sci. Instrum **80**, 94901 (2009).

[3] Y. Cho, C.S. Chang, K. Lee, M. Gong, K. Nomoto, M. Toita, L.J. Schowalter, D.A. Muller, D. Jena, and H.G. Xing, Cite as Appl. Phys. Lett **116**, 172106 (2020).

[4] K. Lee, Y. Cho, L.J. Schowalter, M. Toita, H.G. Xing, and D. Jena, Appl. Phys. Lett. **116**, 262102 (2020).

[5] J. Yang, E. Ziade, and A.J. Schmidt, Rev. Sci. Instrum. **87**, (2016).

[6] W. Shen, D. Vaca, and S. Kumar, Nanoscale Microscale Thermophys. Eng. (2020).